UC Davis
UC Davis Previously Published Works

Title

Wavefront sensorless adaptive optics optical coherence tomography for in vivo retinal imaging in mice.

Permalink

https://escholarship.org/uc/item/0c54h38s

Journal

Biomedical Optics Express, 5(2)

ISSN

2156-7085

Authors

Jian, Yifan
Xu, Jing
Gradowski, Martin A
et al.

Publication Date

2014-02-01

DOI

10.1364/boe.5.000547

Peer reviewed

Wavefront sensorless adaptive optics optical coherence tomography for *in vivo* retinal imaging in mice

Yifan Jian,[1] Jing Xu,[1] Martin A. Gradowski,[1] Stefano Bonora,[2] Robert J. Zawadzki,[3,4] and Marinko V. Sarunic[1,*]

[1]*Engineering Science, Simon Fraser University, Burnaby, BC, V5A 1S6, Canada*
[2]*CNR-Institute of Photonics and Nanotechnology, via Trasea 7, 35131, Padova, Italy*
[3]*Vision Science and Advanced Retinal Imaging Laboratory (VSRI),Department of Ophthalmology & Vision Science, University of California Davis, 4860 Y Street, Ste. 2400, Sacramento, CA 95817, USA*
[4]*UC Davis Eye-Pod, Dept. of Cell Biology and Human Anatomy, University of California Davis,4320 Tupper Hall, Davis, CA, 95616, USA*
[*]*msarunic@sfu.ca*

Abstract: We present wavefront sensorless adaptive optics (WSAO) Fourier domain optical coherence tomography (FD-OCT) for *in vivo* small animal retinal imaging. WSAO is attractive especially for mouse retinal imaging because it simplifies optical design and eliminates the need for wavefront sensing, which is difficult in the small animal eye. GPU accelerated processing of the OCT data permitted real-time extraction of image quality metrics (intensity) for arbitrarily selected retinal layers to be optimized. Modal control of a commercially available segmented deformable mirror (IrisAO Inc.) provided rapid convergence using a sequential search algorithm. Image quality improvements with WSAO OCT are presented for both pigmented and albino mouse retinal data, acquired *in vivo*.

References and links

1. W. J. Donnelly 3rd and A. Roorda, "Optimal pupil size in the human eye for axial resolution," J. Opt. Soc. Am. A **20**(11), 2010–2015 (2003).
2. P. Godara, A. M. Dubis, A. Roorda, J. L. Duncan, and J. Carroll, "Adaptive optics retinal imaging: emerging clinical applications," Optom. Vis. Sci. **87**(12), 930–941 (2010).
3. D. R. Williams, "Imaging single cells in the living retina," Vision Res. **51**(13), 1379–1396 (2011).
4. B. Hermann, E. J. Fernández, A. Unterhuber, H. Sattmann, A. F. Fercher, W. Drexler, P. M. Prieto, and P. Artal, "Adaptive-optics ultrahigh-resolution optical coherence tomography," Opt. Lett. **29**(18), 2142–2144 (2004).
5. R. J. Zawadzki, S. M. Jones, S. S. Olivier, M. Zhao, B. A. Bower, J. A. Izatt, S. Choi, S. Laut, and J. S. Werner, "Adaptive-optics optical coherence tomography for high-resolution and high-speed 3D retinal in vivo imaging," Opt. Express **13**(21), 8532–8546 (2005).
6. Y. Zhang, B. Cense, J. Rha, R. S. Jonnal, W. Gao, R. J. Zawadzki, J. S. Werner, S. Jones, S. Olivier, and D. T. Miller, "High-speed volumetric imaging of cone photoreceptors with adaptive optics spectral-domain optical coherence tomography," Opt. Express **14**(10), 4380–4394 (2006).
7. R. J. Zawadzki, S. M. Jones, S. Pilli, S. Balderas-Mata, D. Y. Kim, S. S. Olivier, and J. S. Werner, "Integrated adaptive optics optical coherence tomography and adaptive optics scanning laser ophthalmoscope system for simultaneous cellular resolution in vivo retinal imaging," Biomed. Opt. Express **2**(6), 1674–1686 (2011).
8. O. P. Kocaoglu, S. Lee, R. S. Jonnal, Q. Wang, A. E. Herde, J. C. Derby, W. Gao, and D. T. Miller, "Imaging cone photoreceptors in three dimensions and in time using ultrahigh resolution optical coherence tomography with adaptive optics," Biomed. Opt. Express **2**(4), 748–763 (2011).
9. D. X. Hammer, R. D. Ferguson, M. Mujat, A. Patel, E. Plumb, N. Iftimia, T. Y. P. Chui, J. D. Akula, and A. B. Fulton, "Multimodal adaptive optics retinal imager: design and performance," J. Opt. Soc. Am. A **29**(12), 2598–2607 (2012).
10. J. W. Evans, R. J. Zawadzki, S. M. Jones, S. S. Olivier, and J. S. Werner, "Error budget analysis for an adaptive optics optical coherence tomography system," Opt. Express **17**(16), 13768–13784 (2009).

11. D. P. Biss, D. Sumorok, S. A. Burns, R. H. Webb, Y. Zhou, T. G. Bifano, D. Côté, I. Veilleux, P. Zamiri, and C. P. Lin, "In vivo fluorescent imaging of the mouse retina using adaptive optics," Opt. Lett. **32**(6), 659–661 (2007).

12. Y. Geng, L. A. Schery, R. Sharma, A. Dubra, K. Ahmad, R. T. Libby, and D. R. Williams, "Optical properties of the mouse eye," Biomed. Opt. Express **2**(4), 717–738 (2011).

13. Y. Geng, A. Dubra, L. Yin, W. H. Merigan, R. Sharma, R. T. Libby, and D. R. Williams, "Adaptive optics retinal imaging in the living mouse eye," Biomed. Opt. Express **3**(4), 715–734 (2012).

14. A. Jesacher, and M. J. Booth. "Sensorless adaptive optics for microscopy," in SPIE MOEMS-MEMS (Olivier, S. S., Bifano, T. G. & Kubby, J. A.) 79310G–9 (2011).

15. H. Hofer, N. Sredar, H. Queener, C. Li, and J. Porter, "Wavefront sensorless adaptive optics ophthalmoscopy in the human eye," Opt. Express **19**(15), 14160–14171 (2011).

16. D. P. Biss, R. H. Webb, Y. Zhou, T. G. Bifano, P. Zamiri, and C. P. Lin. "An adaptive optics biomicroscope for mouse retinal imaging," in Proc. SPIE **6467**(1), 646703 (SPIE, 2007).

17. C. Alt, D. P. Biss, N. Tajouri, T. C. Jakobs, and C. P. Lin, "An adaptive-optics scanning laser ophthalmoscope for imaging murine retinal microstructure," Bios **7550**, 1–11 (2010).

18. P. Villoresi, S. Bonora, M. Pascolini, L. Poletto, G. Tondello, C. Vozzi, M. Nisoli, G. Sansone, S. Stagira, and S. De Silvestri, "Optimization of high-order harmonic generation by adaptive control of a sub-10-fs pulse wave front," Opt. Lett. **29**(2), 207–209 (2004).

19. M. J. Booth, "Wavefront sensorless adaptive optics for large aberrations," Opt. Lett. **32**(1), 5–7 (2007).

20. M. Minozzi, S. Bonora, A. V. Sergienko, G. Vallone, and P. Villoresi, "Optimization of two-photon wave function in parametric down conversion by adaptive optics control of the pump radiation," Opt. Lett. **38**(4), 489–491 (2013).

21. R. J. S. Bonora and R. J. Zawadzki, "Wavefront sensorless modal deformable mirror correction in Adaptive Optics - Optical Coherence Tomography," Opt. Lett. **38**(22), 4801 (2013).

22. Y. Jian, R. J. Zawadzki, and M. V. Sarunic, "Adaptive optics optical coherence tomography for in vivo mouse retinal imaging," J. Biomed. Opt. **18**(5), 056007 (2013).

23. C. J. Kempf, M. A. Helmbrecht, and M. Besse. "Adaptive optics control system for segmented MEMS deformable mirrors," in Proc. SPIE 7595, MEMS Adapt. Opt. IV (Olivier, S. S., Bifano, T. G. & Kubby, J. A.) 75950M–12 (2010).

24. Y. Jian, K. Wong, and M. V. Sarunic, "Graphics processing unit accelerated optical coherence tomography processing at megahertz axial scan rate and high resolution video rate volumetric rendering," J. Biomed. Opt. **18**(2), 026002 (2013).

25. J. Li, P. Bloch, J. Xu, M. V. Sarunic, and L. Shannon, "Performance and scalability of Fourier domain optical coherence tomography acceleration using graphics processing units," Appl. Opt. **50**(13), 1832–1838 (2011).

26. J. Schindelin, I. Arganda-Carreras, E. Frise, V. Kaynig, M. Longair, T. Pietzsch, S. Preibisch, C. Rueden, S. Saalfeld, B. Schmid, J.-Y. Tinevez, D. J. White, V. Hartenstein, K. Eliceiri, P. Tomancak, and A. Cardona, "Fiji: an open-source platform for biological-image analysis," Nat. Methods **9**(7), 676–682 (2012).

27. R. A. Muller and A. Buffington, "Real-time correction of atmospherically degraded telescope images through image sharpening," J. Opt. Soc. Am. **64**(9), 1200 (1974).

28. L. Thibos, R. A. Applegate, J. T. Schwiegerling, and V. S. T. M. Webb, Robert. "Standards for reporting the optical aberrations of eyes - OSA Technical Digest," in Vision Science and its Applications **35** 232–244 (Optical Society of America, 2000).

29. D. Debarre, M. J. Booth, and T. Wilson, "Image based adaptive optics through optimisation of low spatial frequencies," Opt. Express **15**(13), 8176–8190 (2007).

30. S. Tuohy and A. G. Podoleanu, "Depth-resolved wavefront aberrations using a coherence-gated Shack-Hartmann wavefront sensor," Opt. Express **18**(4), 3458–3476 (2010).

31. S. A. Rahman and M. J. Booth, "Direct wavefront sensing in adaptive optical microscopy using backscattered light," Appl. Opt. **52**(22), 5523–5532 (2013).

32. M. Shaw, K. O'Holleran, and C. Paterson, "Investigation of the confocal wavefront sensor and its application to biological microscopy," Opt. Express **21**(16), 19353–19362 (2013).

33. J. Wang, J.-F. Léger, J. Binding, A. C. Boccara, S. Gigan, and L. Bourdieu, "Measuring aberrations in the rat brain by coherence-gated wavefront sensing using a Linnik interferometer," Biomed. Opt. Express **3**(10), 2510–2525 (2012).

34. R. J. Zawadzki, S. S. Choi, S. M. Jones, S. S. Oliver, and J. S. Werner, "Adaptive optics-optical coherence tomography: optimizing visualization of microscopic retinal structures in three dimensions," J. Opt. Soc. Am. A **24**(5), 1373–1383 (2007).

1. Introduction

Adaptive optics (AO) was originally developed to correct for the perturbations of star light passing through the atmosphere that affected the resolving power of large pupil diameter optical telescopes. Over the last fifteen years, adaptive optics has also been integrated into ophthalmoscopes and microscopes for retinal and biological tissue imaging, correcting monochromatic optical aberrations and allowing diffraction limited imaging. AO is required

for retinal imaging in humans when the pupil is larger than 3mm [1], to achieve diffraction limited performance using fundus photography, scanning laser ophthalmoscopy (SLO), or optical coherence tomography (OCT) [2,3]. To better visualize the cellular microstructure and to understand the molecular processes in living retinas, high resolution retinal imaging is desired. Diffraction limited high resolution imaging can be achieved with AO incorporated into the sample arm of an OCT system [4–9].

Most AO systems use a wavefront sensor (WFS) which measures the wavefront aberrations, and compensate for them with a wavefront corrector, usually a deformable mirror (DM). The performance of an AO system is limited by the accuracy of the wavefront sensor, and there are various sources of error which lead to imperfect correction of wavefront aberrations [10]. Additionally, wavefront sensing can suffer from non-common path errors, misalignment, detected spot centroiding and wavefront reconstruction errors, back-reflection from lens based systems, etc. Moreover, these issues are exacerbated in small animal retinal imaging systems. Biss et al. demonstrated that with AO correction of monochromatic aberrations, the brightness and resolution of the image can be increased in mouse retinal imaging with SLO [11]. However, they also reported on the difficulties of wavefront sensing for mice, which may arise from the 'small eye artifact'. Geng et al. demonstrated the appearance of a double spot in the wavefront sensor (WFS) when the wavefront beacon with a long depth of focus was reflected from the mouse retina, in contrast to a single spot when focusing on a retinal vessel [12]. The latest work from Geng et al. showed exciting results for AO cSLO in a mouse retina *in vivo*, where the wavefront sensing beam was kept in focus on the outer retina to obtain reliable and accurate the wavefront measurements [13]. However, the approach used in these reports on wavefront sensing is likely limited to pigmented mice, and would not likely perform as well in the presence of strong back reflection from the choroid in albino animals.

In order to resolve the issues associated with the Shack-Hartmann wavefront sensing and to extend the applications of AO imaging systems, wavefront sensorless adaptive optics (WSAO) systems have been developed and successfully demonstrated in microscopy and retinal imaging for both humans and mice [14–17]. These reports have shown that WSAO imaging systems can achieve comparable performance as those with wavefront sensor control. Many different WSAO control algorithms have been extensively investigated and discussed [18–20], and can be separated into two main categories: stochastic and imaged-based. Bonora and Zawadzki recently reported on a modal control WSAO OCT system capable of optimizing low order Zernike terms [21], and proposed the possibility of extending the technology for real-time *in vivo* imaging.

The purpose of this report is to investigate the combination of WSAO with FD-OCT, enabling selection of the axial position of the AO-system focus using the OCT B-scans, and thus allowing AO correction at the structure of interest. We present a novel modal control WSAO OCT system for small animal retinal imaging, which enables correction of aberrations up to the fifth radial Zernike orders for user-selected layers in real-time. *In vivo* retinal imaging of pigmented and albino mice is presented, and the image quality improvement resulting from AO correction is demonstrated.

2. Method

2.1 AO FD-OCT engine

Our previously reported lens based AO-OCT system was modified for this project, and the details are presented in Fig. 1. The same light source, spectrometer, and deformable mirror (DM) were used as reported in the manuscript describing our previous AO-OCT system [22]. The spectrometer was custom built with a high speed line scan CMOS camera (Bioptigen, Inc, Durham, NC). The IrisAO segmented MEMS DM (PT111, Iris AO, Inc, Berkeley, CA) was factory-calibrated for accurate open-loop operation for modal control [23]. Due to the

wavefront sensorless operation, back-reflection from the lenses was no longer a concern for the AO subsystem, and the mechanical tilt of the lenses was removed to minimize the system aberrations. Removal of restrictions connected with use of the wavefront sensor allowed us to increase the numerical aperture from 0.14 NA up to 0.21 NA. The relatively small (5μm) stroke of our DM was sufficient for wavefront correction because the use of the fundus lens reduced the low order aberrations and permitted manual adjustment of the focus [22]. The estimated focal width (Gaussian waist $1/e^2$) for our imaging beam was 1.3 μm in air and had a corresponding depth of focus of 12 μm. In order to accommodate the increased NA and pupil size on the objective lens, the 2mm fundus lens (Volk Optical Inc, Mentor, OH) was replaced with a 6mm diameter, −12.5 mm focal length plano-concave lens (KPC013, Newport Instruments, Irvine, CA). The real-time acquisition of rodent retinal volumes consisted of 2048x128x128 pixels (axial points x number of A-scans/B-scan x number of B-scans/volume) with a line rate of 80 kHz during the WSAO optimization stage, and 2048x360x360 pixels with a line rate of 90 kHz for the final data acquisition and saving stage. The increased acquisition speed compared to our previous report helped to significantly reduce motion artifacts when imaging the mouse retina *in vivo*.
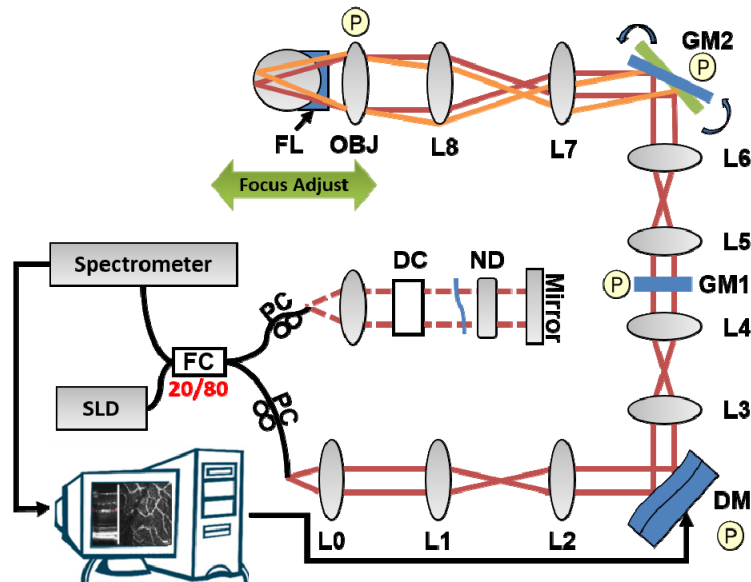

Fig. 1. Schematic of the WSAO FD-OCT system: DC - dispersion compensation; DM - deformable mirror; FC - 20/80 fiber coupler, 20% of the light from SLD goes to sample arm, 80% goes to reference arm; GM1, GM2 - horizontal and vertical galvo scanning mirrors; FL - fundus lens; PC - polarization controller. SLD - superluminescent diode; L - achromatic lenses: L0: (f = 16mm); L1, L2: (f = 300mm); L3, L4: (f = 200mm); L5, L6: (f = 150mm); L7, (f = 100mm) L8: (f = 300mm); OBJ - objective: (f = 25mm); ND - neutral density filter; P represents the location of the planes conjugated to the pupil throughout the system. GM1 is slow scan mirror and is presented unfolded for clarity. Note that the schematic is drawn for illustrative purposes only; it does not reflect the actual physical dimensions of the system.

A custom written program for FD-OCT acquisition with GPU accelerated processing [24,25], was modified for this project. The updated software is able to generate an *en face* view from the layers of interest, selected by the operator in the OCT B-scan window. Advanced camera controls offer the ability of seamlessly changing the image acquisition parameters, such as the A-scan line rate and sampling rate, in real-time. The DM control functions, whose implementation was based on the IrisAO API, were incorporated into the software for fully automated WSAO. The entire WSAO OCT system requires only one PC and one operator. The OCT processing steps (resampling, numerical dispersion

compensation, and FFT) were performed on the GPU [24]. The CPU was used for coordinating data acquisition, configuring the camera via serial control, and synchronizing the scanner (6210H, Cambridge Technology Inc., Lexington, MA) with the camera and frame grabber (PCIe-1433, National Instrument, Austin, TX). The CPU also controlled the AO optimization. During the optimization stage, the time to update the DM through the controller (Smart Driver II - 128, IrisAO, Inc, Berkeley, CA) was ~7.1ms.

Data saved during acquisition was written to binary files as unprocessed interferograms. The saved data was processed in Matlab (Mathworks, Inc, Natick, MA) with standard OCT processing (resampling, numerical dispersion compensation, and FFT) for presentation; there was no additional post processing done on the images. Measurement and analysis of the image data was performed using Amira (FEI Visualization Sciences Group, Burlington, MA), and Fiji [26].

2.2 Imaged based wavefront sensorless adaptive optics modal optimization algorithm

The WSAO optimization process was initialized with manual selection of the axial position (depth range, Δz) of the retinal layer of interest in the B-scan display window of the software. An OCT *en face* image was generated from the user selected region using maximum intensity projection; the brightness of this 2D *en face* image was calculated by summing the intensity of each pixel, and was used as the merit function $J(\mathbf{k})$ as formulated in Eq. (1) [27]:

$$J(\mathbf{k}) = \sum_{x,y} \left(\max_{\Delta z} \left(I^{w(\mathbf{k})}(x, y, z) \right) \right),$$ (1)

where $\mathbf{k}$ is vector of the Zernike coefficients; x, y and z are coordinates in image space; and $I^{w(\mathbf{k})}$ is the intensity of the OCT data acquired with the wavefront aberrations $w(\mathbf{k})$ applied to the DM.

The wavefront aberrations $w(\mathbf{k})$ can be represented by a set of orthonormal Zernike polynomials as shown in Eq. (2). The IrisAO DM has software libraries to produce approximations of the shapes corresponding to each Zernike polynomial up to the 5th order in the Zernike expansion [28]. For n Zernike radial modes Z, the wavefront aberration was represented as

$$w(\mathbf{k}) = \sum_{n=3}^{20} k_n Z_n.$$ (2)

The modal WSAO algorithm searches for the coefficients of the Zernike polynomial that produce the highest merit function value, and thus minimizes the optical aberrations as indicated in Eq. (3). The optimized values of the coefficients are denoted as k_i*, and the initial value of the Zernike coefficients are denoted as $k^{(0)}$.

$$k_i^* = \arg \max_{k_i} \left(J \left(k_1^*, k_2^*, \cdots, k_i, \cdots, k_{n-1}^{(0)}, k_n^{(0)} \right) \right),$$

$$k_1^{(0)}, k_2^{(0)}, \cdots, k_n^{(0)} = 0.$$ (3)

Due to the orthogonal nature of the Zernike polynomials, the optimization of each Zernike mode can be performed independently [29]. Our optimization determines the appropriate value of the coefficient for each mode. The first Zernike mode to be optimized is the defocus ($n = 4$) followed by astigmatism ($n = 3, 5$) and then the remaining modes. A flowchart for the WSAO modal optimization algorithm is shown in Fig. 2.

The search for the optimum coefficient began by applying nine linearly spaced values of the Zernike mode coefficient that was being optimized to the DM, with the initial step size determined by prior knowledge. The image intensity merit function corresponding to each of the nine coefficients was acquired and the highest value was found. If there was an improvement in image brightness compared to the last optimized Zernike mode, and the index

of the maximum valued coefficient was near the center of the range of coefficients searched (i.e. 4-6), then the shape was applied to the DM and the optimization algorithm advanced to the next Zernike mode. If the index of the maximum valued coefficient was off centered (i.e. 1-3 or 7-9), then a new linear search commenced with a new linearly spaced steps centered on the maximum valued coefficient. If there was no improvement in image quality after one iteration, the algorithm attempted a non-linear search in the central region, with a finer step size for the nine new Zernike coefficients. The algorithm limited the number of search iterations for each Zernike mode, and after reaching the limit, the algorithm applied the DM shape that produced the best merit function, then moved on to optimize the next Zernike mode. If there was no improvement during the search for specific Zernike mode, the coefficient of that mode was set to zero. Once all Zernike modes were optimized, the adaptive search algorithm terminated.
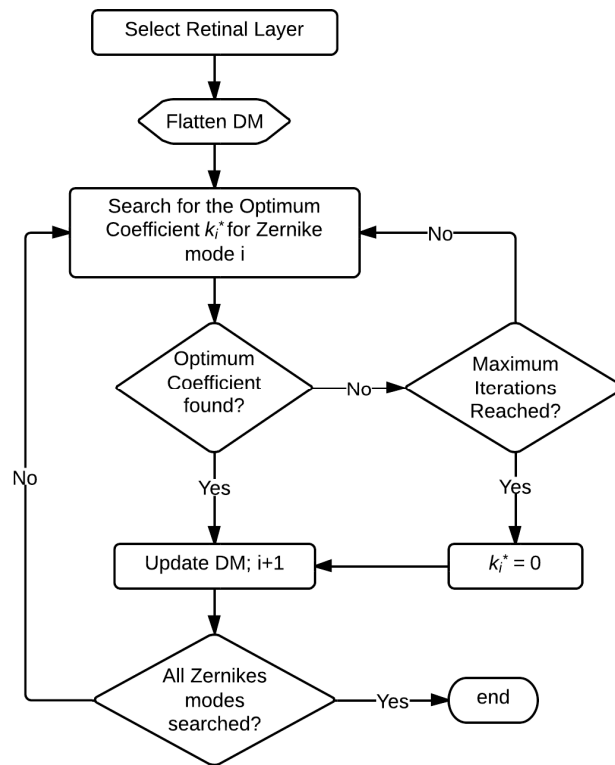

Fig. 2. WSAO search algorithm flowchart. DM – Deformable Mirror; k_i* - the optimized coefficient for Zernike mode i.

2.3 Mouse handling

Mice of strain C57BL/6J (pigmented) and BALB/cByJ (albino) imaged in this report were obtained from Jackson Laboratories (Bar Harbor, ME). All mouse imaging experiments were performed under protocols compliant to the Canadian Council on Animal Care, and with the approval of the University Animal Care Committee at Simon Fraser University. The mice were anesthetized (ketamine, dexmedetomidine, and acepromazine mixture (75:1:1 mg/kg body weight) injected intraperitoneally) and revived after the imaging experiment using atipamezole (1mg/kg). A drop of topical anesthetic (Alcaine) was applied before their pupils were dilated using a topical solution (Tropicamide, 0.8%) prior to imaging. Generous amounts of artificial tear gel (Systane Original, Alcon) were applied in order to maintain

corneal hydration. During the imaging session, the mouse was placed on a stage with a bite bar, then the eye was aligned so that it was coupled into the fundus lens with gentle contact. Each imaging session lasted ~30 minutes. The optical power at the mouse eye was ~750µw. The maximum time (number of iterations) for the WSAO optimization was fixed; however, the actual number of iterations was dependent on the aberrations present in each individual mouse. We did not observe any differences in the optimization time between albino and pigmented mice. The results presented in this manuscript are representative of the imaging sessions with the 7 mice used in this research.

3. Results

3.1 Phantom imaging

The WSAO OCT system was tested and validated by imaging a biological phantom (a leaf) placed at the focus of the objective lens. The optimized Zernike coefficients are shown in Fig. 3, along with the merit function value for each optimized Zernike term. The RMS wavefront of the correction applied was computed from the coefficients of the Zernike polynomial determined through our WSAO algorithm. The final resultant wavefront had an RMS of 52.2nm, which is smaller than $\lambda/14$ (the Maréchal criterion for a diffraction limited optical system). Note that in the Zernike plot of Fig. 3, the merit function decreased after the optimization of the Zernike mode 16; this could be caused by system errors such as laser power fluctuation and interferometric instability due to the long optical path (~3.5m).
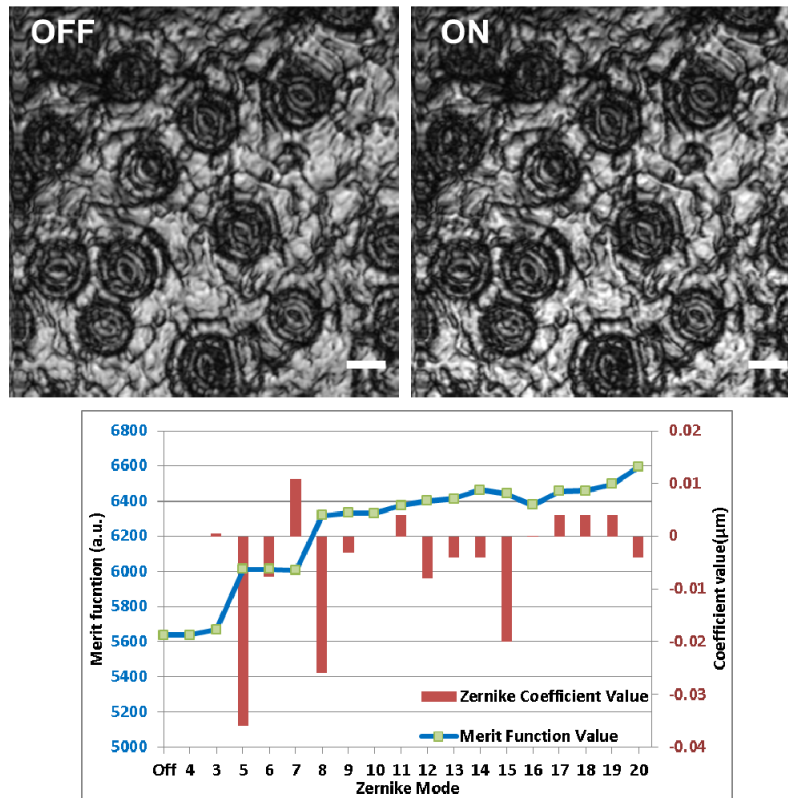

Fig. 3. OCT images of a leaf with and without WSAO corrections. Bottom figure: (blue line graph) The summed intensity (merit function value) of *en face* images after optimization of each Zernike mode. (red bar graph) The optimized Zernike coefficient value for each Zernike mode. Scale bar: 20µm. The Zernike coefficients follow the OSA standard for reporting the optical aberrations of eyes.

Figure 4 shows the merit function during the optimization process starting from optimizing of the defocus term (n = 4), then the rest of the Zernike terms in increasing order. For demonstration purposes, only the first search iteration for 8 Zernike modes were shown. The merit function for each Zernike mode typically forms a convex shape that is suitable for the optimization algorithm.
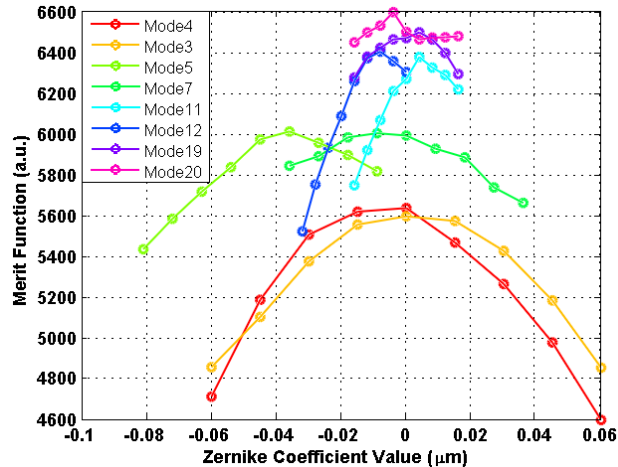

Fig. 4. Merit function during the optimization process. Only the first search iteration of 8 Zernike modes are shown for clarity of the presentation, further iterations resulted in an increased value of the merit function for some of the terms. The data presented in Fig. 3 were obtained after the complete optimization process.

3.2 Pigmented mouse retinal imaging

The first step in mouse imaging was to use a cross-aiming scan pattern in order to facilitate the alignment, and to ensure that the retina layers were perpendicular to the incident beam. Next, the layer of interest (Nerve Fiber Layer, NFL in this case) was manually placed at the focus of the OCT by translating the combination of mouse and fundus lens relative to the fixed objective. The layer of interest was highlighted by the operator in the OCT B-scan window within the two red lines. The program then generated the *en face* view of the selected layer by maximum intensity projection, and calculated the sum of pixels in the *en face* view, corresponding to the image intensity merit function. Note that the OCT B-scan was displayed in a linear scale. Prior to the WSAO optimization, the low resolution (128 x 128, ~4.6 vol/s) scanning pattern was chosen, and the DM was flattened. All 18 Zernike terms were optimized in 33 iterations, with each iteration consisting of 9 steps. The whole process took ~65 seconds. Figure 5 is a screen capture from a video (Media 1) that was recorded during an *in vivo* imaging session of a pigmented mouse to demonstrate the WSAO OCT optimization process. For illustration purposes, the video was sped up by a factor of 4. The increase in image brightness and contrast can clearly be observed as the Zernike terms were optimized. Nerve fiber bundles, a blood vessel, and capillaries can be easily differentiated as the flow in the blood vessel and capillaries was clearly visualized. After WSAO optimization, the scanning pattern was switched to high resolution (360x360pixels) mode visualization and for saving data. Volumes of various fields of view with wavefront optimized (AO ON), as well as volumes with the DM flattened (AO OFF), were saved for comparison purposes.
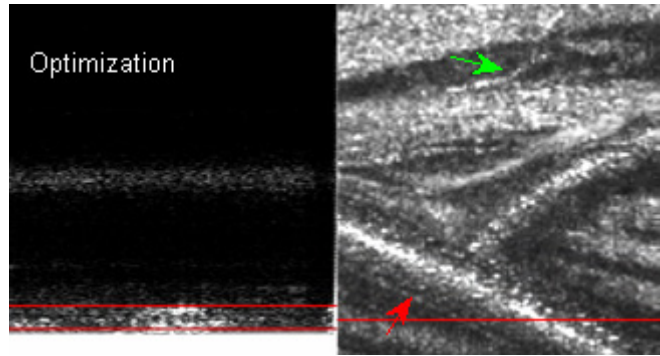
Fig. 5. Screen capture of an imaging session of a pigmented mouse (Media 1). The first part of the video presents the WSAO optimization on the nerve fiber layer with a low resolution scanning pattern. The field of view (170x170 µm) was close to the optic nerve head as indicated by the converging nerve fibers. The green arrow points to a capillary and the red arrow points to the edge of the blood vessel wall. The second part of the video that shows the high resolution images is displayed at 2x the acquisition speed, and the field of view was changed to 250x250 µm and 333x333 µm during acquisition.

Images extracted from these volumes are presented in Fig. 6; the orientation of the B-scan was inverted relative to Media 1. The *en face* images of the NFL were extracted from the OCT volumes at the locations indicated on the B-scan. As mentioned above, for these images, the focal plane was manually placed on the inner retina before WSAO optimization by moving the fundus lens and mouse relative to the fixed objective lens. Not only did the overall image contrast and brightness increase, but more importantly, features such as the capillaries above the nerve fibers and the blood vessel wall around the large vessel at the bottom of the image became more visible and well-defined after AO correction. Figure 6(e) shows the summed intensity merit function value (blue line graph) of *en face* images after optimization of each Zernike mode, and the optimized Zernike coefficient value for each Zernike mode (red bar graph). The defocus term (mode 4) provided approximately 40% of the improvement in the image intensity, whereas correction of the high order aberrations (modes 6 and greater) provided approximately 45% of the total intensity improvement.
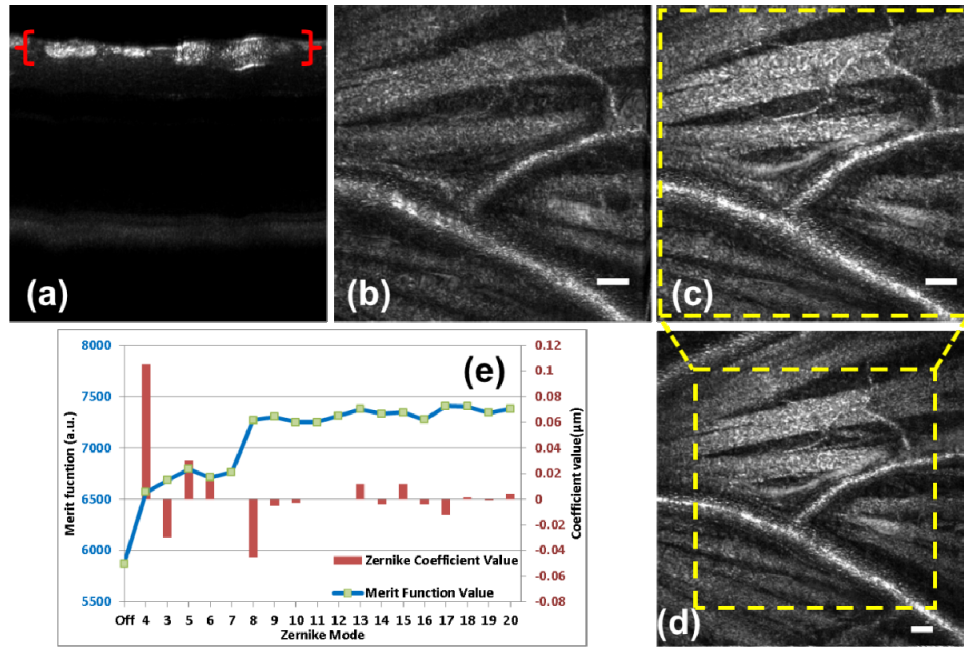
Fig. 6. WSAO OCT images of NFL of a pigmented mouse. (a) OCT B-scan in linear scale, emphasizing the location and depth of focus of the imaging beam at the NFL. (b-d) *En face* projection of the nerve fiber layer (generated within the red brackets in (a)) before (b) and after (c) WSAO optimization. (d) was acquired with a larger field of view after WSAO optimization. (e) (Blue line graph) The summed intensity (merit function value) of *en face* images after optimization of each Zernike mode. (Red bar graph) The optimized Zernike coefficient value for each Zernike mode. The RMS of the wavefront applied by the DM is 0.125μm. Scale bar: 25μm.

3.3 Albino mouse retinal imaging

The lack of pigment in the RPE layer of albino mice results in large and blurry spots when using conventional wavefront sensing. With WSAO OCT, no wavefront sensing is needed, and there is essentially no difference between imaging the inner retina of pigmented versus albino mice. Images acquired *in vivo* from an albino mouse with the WSAO OCT are presented in Fig. 7. With the AO activated, the layer of interest (Outer Plexiform Layer, OPL) was selected and the aberration correction optimization was performed to obtain the best wavefront correction at that layer. The improvement in image quality with WSAO correction can be seen qualitatively in Fig. 7 through sharper lines and brighter features (indicative of an improvement in resolution). A quantitative comparison of the increase in brightness and sharpness of the capillaries in the OPL with the WSAO correction is also presented in Fig. 7. For this imaging session, the defocus term (mode 4) provided approximately 12% of the improvement in the image intensity. Similar to the results presented in Section 3.2, correction of the high order aberrations (modes 6 and greater) provided approximately 40% of the total intensity improvement.
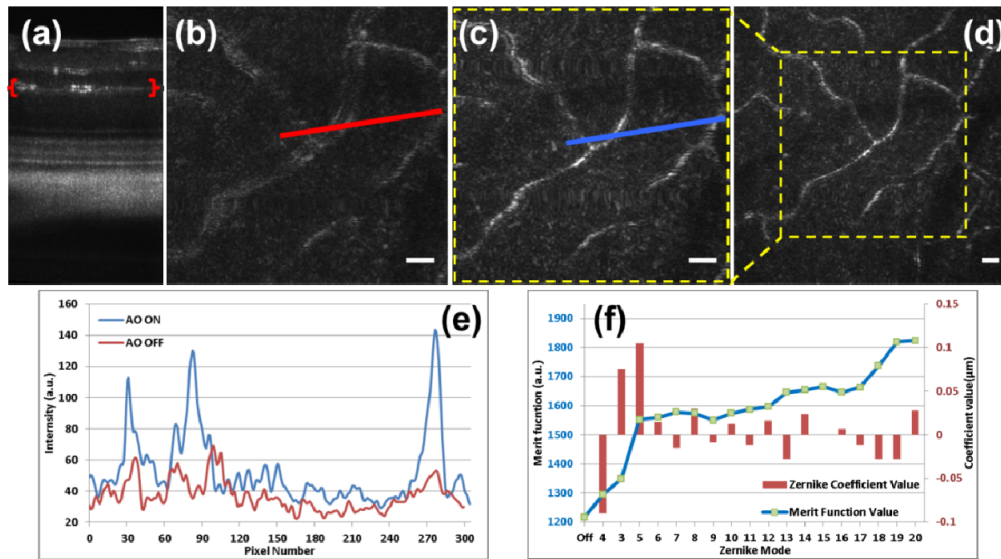
Fig. 7. (a) Cross sectional images of the albino mouse retina acquired *in vivo* with the sensorless WSAO OCT system presented on a linear scale. The axial depths indicated by the brackets represent the location of the *en face* projection of the retinal layers of interests with AO-OFF (b) and AO-ON (c,d). Scale bar: 20μm. (e) The effect of AO correction is demonstrated by comparing the signal intensity across lines taken from the *en face* images at locations (b, red) and (c, blue). (f) (Blue line graph) The summed intensity (merit function value) of the *en face* images after optimization of each Zernike mode. (Red bar graph) The optimized Zernike coefficient value for each Zernike mode. The RMS of the wavefront applied by the DM is 0.175μm.

4. Discussion

Adaptive optics wavefront error correction is an active research area. The performance of the adaptive optics system largely depends on the reliability and accuracy of the wavefront aberration measurements. The issue is further complicated with strongly scattering and multi-layered samples. Many different techniques have been investigated, such as coherence-gated and confocal wavefront sensing, to name a few [13,30–32]. Wavefront sensorless AO offers a more direct solution. Instead of relying on wavefront aberration measurement from the Shack-Hartmann wavefront sensor as feedback to the AO loop, wavefront sensorless AO analyzes merit functions based on the image (such as image intensity), then iteratively searches for the optimal Zernike modes to apply to the DM.

WSAO OCT provides a practical and promising way to achieve depth resolved aberration correction that does not rely on a wavefront sensor. The WSAO system presented in this report has several advantages over a conventional AO system with wavefront sensor control: it reduces the system complexity and cost, it is immune to the wavefront sensor centroid and reconstruction error, non-common path error, and back-reflection in a lens based system. Lower light levels can be achieved, since there is no consumption of the signal light for wavefront sensing. More importantly, because WSAO OCT detects coherence gated ballistic photons with high SNR, it allows aberration correction in situations when the images have low intensity, or when the layer of interest is obscured by other surfaces in the object. This is the case for mouse retinal imaging, in particular for albino strains where scattering from the choroid dominates. Furthermore, since the OCT provides a cross-sectional view of the retina, our sensorless AO enables aberration correction for user-selected layers in real-time. The capability of depth resolved aberration correction may also be very beneficial for other applications such as deep tissue imaging in brain [33].

We demonstrated WSAO OCT for mouse retinal imaging of structures like nerve fiber bundles, capillaries and a blood vessel wall in pigmented and albino animals. To the best of our knowledge, only Geng et al [13] demonstrated *in vivo* imaging of the photoreceptor mosaic in a pigmented mouse eye with an AO SLO system that had two times higher resolution than the system presented in this report. Increasing the NA of the current system by a factor of two would decrease the depth of focus to be comparable to the coherence length of the source. Our future work includes the investigation of techniques to extend the depth of focus of high NA imaging with OCT. An increased NA would also increase the amplitude of the aberrations, but that could be mitigated by the use of a deformable mirror with more segments and a larger stroke or a woofer-tweeter configuration [34].

The iterative WSAO aberration correction algorithm is inherently slower than systems with a wavefront sensor that provide direct wavefront measurement. A main challenge of implementing a WSAO imaging system for *in vivo* imaging is the requirement to keep the aberrations relatively static by reducing the subject motion. In our mouse retinal WSAO OCT imaging system, the fundus lens coupled with the mouse eye not only helped to keep the cornea hydrated, but it also reduced the low order aberrations and facilitated alignment. More importantly from the WSAO perspective, it kept the aberrations of the mouse eye static, which allowed the WSAO correction to converge. Furthermore, the anesthetic prescription provided a deeper plane of anesthesia and the increased OCT acquisition speed significantly reduced the motion artifacts when imaging the mouse *in vivo.* As indicated in Media 1, the eye motion was confined to tens of microns both axially and laterally. The residual small motion while imaging the mouse retina *in vivo* is likely the cause of the slight decrease in image intensity after the optimization of some Zernike modes (Fig. 6(e) Zernike modes 6 and 16, and Fig. 7(f) Zernike modes 9 and 16). Therefore, our current WSAO implementation is not yet suitable for imaging living human retinas due the dynamic nature of the tear film and constant motion of the human eye.

The converging speed of the WSAO is limited by several factors. Currently, the WSAO OCT operates at 600 B-scans per second, equivalent to ~4.6 volumes per second at our volume size. We could potentially increase the acquisition imaging speed by a factor of 2 by reducing the A-scan length to 1024 pixels per A-scan. In order to further shorten the WSAO converging time, improvements to the optimization algorithm also need to be investigated. We will also explore different merit functions, such as low frequency components in the Fourier domain, and their relationship with the Zernike modes.

5. Conclusion

We presented a wavefront sensorless adaptive optics OCT system that overcomes the issues associated with conventional Shack-Hartmann wavefront sensing in mice, by directly using the image quality data as a merit function for aberration correction. Furthermore, our wavefront sensorless AO approach facilitates the use of a lens based OCT system, which greatly reduces the system complexity. A GPU processing platform was used to accelerate Fourier domain OCT processing for real-time extraction of intensity information from specific retinal layers in the acquired volume. A modal approach of optimizing Zernike terms on the segmented MEMS-based DM was used in combination with an adaptive search algorithm to provide rapid convergence. Images of both pigmented and albino mouse retinas acquired using WSAO OCT system *in vivo* demonstrated improvement in image brightness and feature sharpness. We have demonstrated coherence gated depth resolved AO correction in user selected retinal layers. Combination of WSAO with OCT allows for precise optimization of the image of the structure at the pre-set depth.

Acknowledgment